Proceedings World Geothermal Congress 2020+1
Reykjavik, Iceland, April - October 2021

Ground Deformation at the Los Humeros Geothermal Field (Mexico) Inferred by InSAR

Eszter BÉKÉSI[1]*, Peter A. FOKKER[1,2], Jon LIMBERGER[1], Joana ESTEVES MARTINS[2], Jan-Diederik VAN WEES[1,2]

* Department of Earth Sciences, Utrecht University, Princectonlaan 8, 3584 CB Utreccht, Netherlands

e.bekesi@uu.nl

Keywords: Enhanced geothermal systems, Ground deformation, Induced seismicity, Inversion

ABSTRACT

Surface deformation can be detected with satellite-based geodetic sensors, providing important insights on subsurface geomechanical properties. In this study, we use Interferometric Synthetic Aperture Radar (InSAR) observations to measure ground deformation due to fluid extraction and due to an induced seismic event at the Los Humeros Geothermal Field (Puebla, Mexico).

The result of the PS-InSAR (Persistent Scatterer by Synthetic Aperture Radar Interferometry) analysis shows that the subsidence at the LHGF was up to 8 mm/year between April 2003 - March 2007, which is small relative to the produced volume of $5x10^6$ m^3/year. The subsidence pattern indicates that the geothermal field is controlled by sealing faults separating the reservoir into several blocks. Our models imply small volume changes in the reservoir and the different nuclei of strain solutions differ only slightly. These findings suggest that the pressure within the reservoir is well supported and that reservoir recharge is taking place.

The occurrence of induced seismicity is independent evidence for the development of effective stresses. The inversion of the coseismic deformation due to the 8 February 2016, Mw 4.2 earthquake showed activation of a shallow normal fault in a reverse manner. Even with the limited compaction observed from the subsidence, the stress development was enough to induce seismicity. Pore pressure contrasts over a fault will increase the stress development. However, the fault structure will be more complex than assumed in the present study, because an acceptable joint match of ascending and descending surface movement data was not possible. An integrated study into the complex reservoir behaviour and the associated stress development over complex faults is therefore warranted.

1. INTRODUCTION

The deployment of DInSAR (Differential Interferometric Synthetic Aperture Radar) allows to detect small movements on the Earth's surface [Hanssen, 2001; Ferretti, 2014]. It utilizes the phase difference between two SAR images to estimate displacement along the satellite line-of-sight (LOS). Higher temporal resolution is achieved using several SAR images and by performing a time-series analysis. This facilitates the monitoring of gradual changes in ground movements using multiple interferograms, while increasing the performance of the phase unwrapping. InSAR is widely used for mapping different geophysical phenomena such as earthquakes, volcanos, landslides, and ground deformation associated with, for instance, subsurface exploration processes [e.g. Atzori et al, 2009].

We have studied surface deformation at the Los Humeros Geothermal field (LHGF) (Fig. 1). The LHGF is among the largest geothermal fields in Mexico, with an installed capacity of ~93.6MW, operated by the national Mexican Electrical company (Comisión Federal de Electricidad, CFE). The LHGF is located inside the quaternary Los Humeros Caldera system, forming the easternmost caldera of the Trans-Mexican Volcanic Belt (Fig. 1) The geothermal reservoir is built up by pre-caldera andesites of Miocene age [Ferriz and Mahood 1984], situated at ~1500 m depth, with an average thickness of ~1000 m [e.g. Carrasco-Núñez et al. 2017]. The geothermal activity is controlled by NNW-SSE to E-W striking structures located inside the caldera (Fig. 1). These active faults induce secondary permeability, providing the path of geothermal fluids associated with active caldera resurgence processes [e.g. Norini et al. 2015].

In this study we have analyzed images acquired by the European Space Agency's (ESA) Envisat satellite between April 2003 and March 2007 to detect surface movements due to field operations and potential discharge and recharge zones. We also looked into deformation derived from the recent Sentinel-1 satellites (2014-2016). We relate ground deformation with volume changes in the reservoir due to injection and production of water, and with co-seismic shear displacement on a fault during an induced earthquake: the 8 February 2016 earthquake along the trace of the Los Humeros fault [Lermo Samaniego et al. ,2016; Santos-Basurto et al. 2018]. The relation between surface deformation and subsurface processes is achieved through analytical solutions for different nuclei of strain. The main goal of this study is to have a better understanding on the subsurface processes at the LHGF based on surface movements. This involves both the reservoir behavior (the pressure distribution within the reservoir and possible reservoir compartmentalization) and the processes leading to the induced seismic event.

[1] University of Utrecht, Geosciences, Earth sciences
[2] ECN-TNO, Applied Geociences

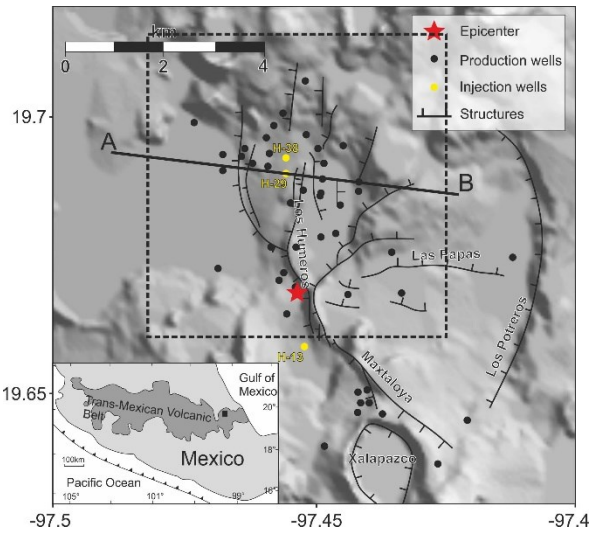

Figure 1 : Major faults, caldera rims, and the location of the wells at the Los Humeros Geothermal Field modified after Norini et al. [2015] and Carrasco-Núñez et al. [2017]. The red star indicates the epicentre of the 8 February 2016, Mw 4.2 earthquake after Lermo Samaniego et al. [2016]. The black dashed rectangle marks the outline of the area selected for modeling.

2. INSAR DATA AND PROCESSING

We performed PS-InSAR time-series analysis to resolve ongoing ground deformation due to geothermal exploration at the Los Humeros geothermal field. We analyzed SLC images (descending track 212) acquired in C-band by ESA's Envisat satellite between April 2003 - March 2007. We selected a subset of 30x35 km covering the Los Humeros caldera system for the time series processing. More information on the procedure can be found in Békési et al [2019a]. We also processed Sentinel-1 (S-1) radar images acquired in wide-swath mode to map the coseismic deformation due to the 8 February 2016, Mw 4.2 earthquake [Békési et al, 2019b]. We use the images of 29 January 2016 and 10 February 2016 for the ascending interferogram. The descending interferogram was processed using the SAR images acquired on 7 February 2016 and on 19 February 2016. The interferometric processing was performed using the GAMMA software [Wegmüller and Werner 1997]. For the coseismic deformation, the area near the surface rupture of the fault was masked out because of the high potential for unwrapping errors resulting from the lack of coherence.

3. MODELLING

Subsurface extraction or injection processes induce movements on the ground surface with variable amplitude through poroelastic coupling. Volume changes in the subsurface result in pressure changes leading to compaction or dilation strain, which is a function of elastic strength or of the compaction coefficient. Furthermore, injection processes can additionally generate thermoelastic effects due to the temperature difference between the injected fluid and reservoir. When cold fluids are injected into the reservoir, temperature near the injection wells drops, leading to thermal contraction. The changed stresses in the reservoir and around it can also induce seismic events when a critical stress on a fault is exceeded.

We related subsidence with fluid extraction from the geothermal field through influence functions. We used nuclei of strain solutions for point sources in an elastic half-space based on a center of compression [Mindlin, 1936] and a tensile, horizontally oriented fault (opening in vertical direction). In case of the center of compression we used the equation after Segall [2010] to calculate the displacement vector at the surface. For the tensile sources we followed Okada [1985] to calculate the displacement vectors at the surface. The equation contains the same parameters as the one for the center of compression, including the coordinates describing the location of the source, the Poisson's ratio of the elastic half-space, and the volume change associated with the tensile dislocation. We tested two configurations for the modeling: first we performed the fitting along an optimized section with a sufficient number of PS, then we modeled the northern part of the field area, where a clear subsidence signal was observed. We placed three sources according to the location of the production and the injection wells. We located the sources at the main extraction/injection depth of 1650 m. The layout of the sources is illustrated in Figure 2. The easternmost and westernmost sources employ contraction due to production, while the middle one uses expansion as a result of injection. The centers of the sources are located 700 m and 800 m from each other. For the coseismic deformation we employed the solution by Okada [1985] for a fault with uniform slip.

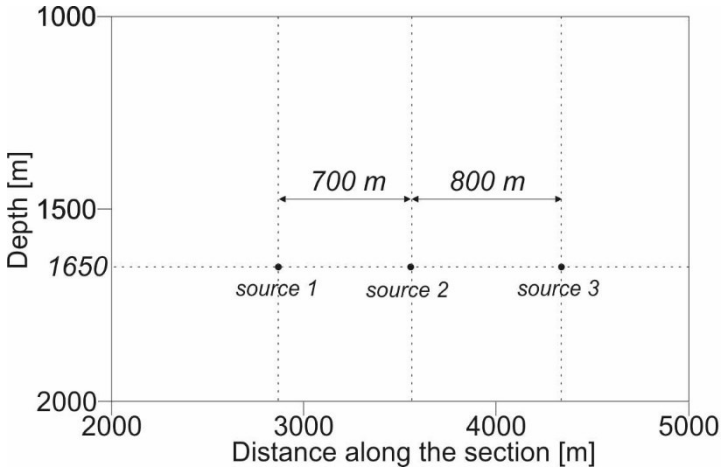

Figure 2. Illustration of the layout of the sources along the cross section. For the trace of the section see Figure 1.

For the layout of the modeled area covering the northern part of the geothermal field area, we used 7 sources in total: 6 contraction sources and 1 expansion source placed between the two injectors. We employed nuclei of strain solutions for inflation/deflation point sources (model 3) and for tensile point sources opening in vertical direction (model 4), equivalent to the sources used for model 1 and model 2, respectively.

The fitting parameters were the volume changes attributed to the sources. We minimized the weighted sum of the residuals using the standard deviations of the LOS velocity estimates to construct the weighting factors. The RMS values in case of all models are below 1 (Table 1), suggesting that the fits are reasonably good.

Table 1: Description of the models, the best fitting volume changes attributed to the sources, and the average yearly produced and injected volumes. Note that the volume changes are reported for the period of one year.

Model results along the cross-section (including 81 PS observations)						
	Description	Depth [m]	Volume change [10^4 m^3] attributed to source 1	Volume change [10^4 m^3] attributed to source 2	Volume change [10^4 m^3] attributed to source 3	RMS
Model 1	Inflation/ deflation point sources	1650	0.0	2.6	-5.8	0.64
Model 2	Tensile point sources	1650	-2.3	1.2	-4.3	0.59

Areal model results for the northern part of the LHGF (including 1337 PS observations)				
	Description	Depth [m]	Total volume change attributed to the 7 sources [10^4 m^3]	RMS
Model 3	Inflation/deflation point sources	1650	-10.0	0.74
Model 4	Tensile point sources	1650	-5.5	0.83

Average yearly produced and injected volumes during the period of the InSAR based on well data provided by CFE	
Total produced volume for one year period [10^4 m^3]	Total injected volume for one year period [10^4 m^3]
~500	~50

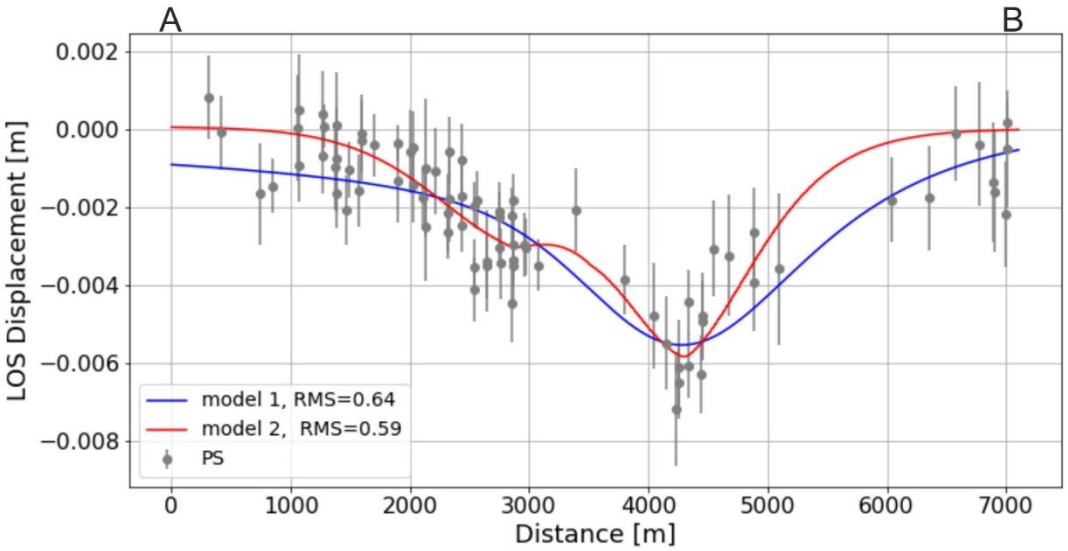

Figure 3. The best fitting influence functions derived from the nuclei of strain solutions along the cross section. Model 1: inflation point sources, model 2: vertical tensile point sources. The PS observations and their standard deviations marked by error bars are plotted in both figures. Note that the LOS displacements are reported for the period of one year. For the trace of the section see Figure 1.

Figure 3 shows the responses derived from the strain nuclei placed at 1650 m depth along the cross section. A good fit was achieved by the tensile point source (model 2). The misfits are a bit larger for the inflation sources (model 1), the influence function is wider and also slightly less deep. Furthermore, the strength of the westernmost source is negligible in contrast with the production data. The error estimates around the InSAR observations corresponds to the standard deviation of the mean velocity estimates. The maximum standard deviation estimated in our area of interest is ~1.5 mm/year.

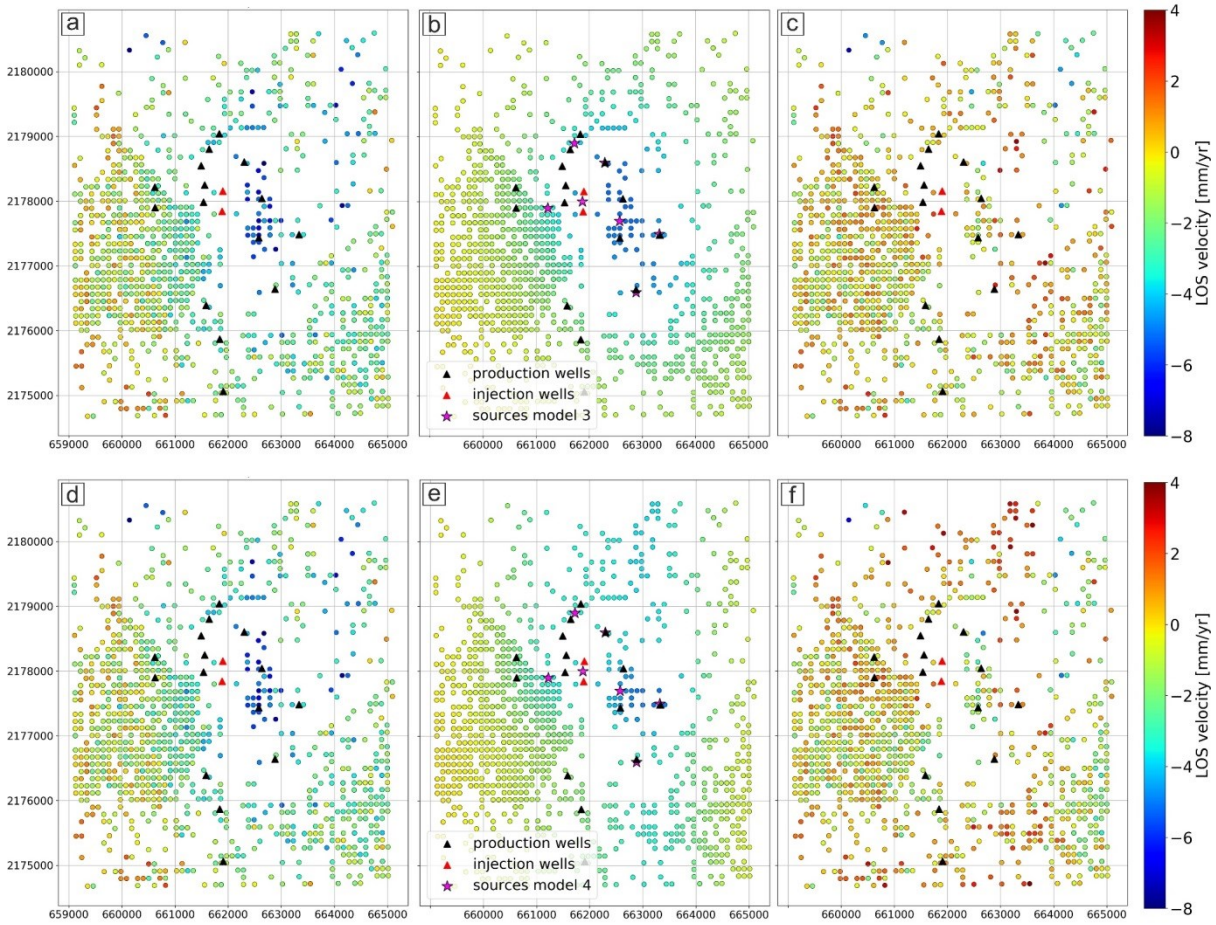

Figure 4. Observed (a, d), modeled (b, e), and residual (c, f) movements in the LOS direction in mm/yr. The coordinates are in UTM zone 14N. The outline of the modeled area is shown in Figure 1.

Figure 4 illustrates the modeling results of the northern part of the field. In contrast with the results through the section, the inflation point sources (model 3) are fitting better than the vertical tensile sources (model 4). The extent and geometry of the subsiding area only slightly differ (Figure 4b and 4e).

For the coseismic deformation during the earthquake in 2016 we performed the modelling using the ascending and descending interferograms separately and with the combination of the two datasets. We inverted the single datasets with the motivation to map the source parameters that better fit with the ascending and descending data separately. Prior to the modelling, InSAR data were subsampled, because the high density of the PS points would require a computationally expensive inversion. Areas with large phase variance are subdivided more finely, and areas with low variance remain coarser. Our datasets covering approximately 8x8 km are resampled to 223 and 217 data points for the ascending and descending interferograms, respectively (Fig. 5).

The inversion targeted a forward model for a rectangular dislocation with nine adjustable parameters. The source parameters are the length, width, depth of the midpoint of the upper edge, dip angle (negative due to dipping to the west), strike (clockwise from north), X and Y coordinates of the midpoint of the upper edge, and the amount of the uniform slip in the strike and dip directions. We selected lower and upper bounds for the source parameters according to prior information about the activated fault based on the observed ground movement pattern and previous studies including geological mapping [e.g. Norini et al. 2015] and seismological data [Lermo Samaniego et al. 2016]. Constraints on the magnitude of slip were set conforming to the amplitude of surface movements inferred from the InSAR data. Bounds were chosen identical for all models and are listed in Table 2.

Our modelling results of the surface deformation due to the 8 February 2016 earthquake at the LHGF are summarized in Table 2 and Figure 5. Surface movements predicted by the three models are consistent with a NNW-SSE-strike, westward-dipping reverse fault with minor strike-slip component (Table 2). However, the geometry of the fault varies for each model. In case of Model 1 and Model 3, the fault extends from the surface down to 1100-1300 m depth. Model 2 predicts a vertical fault plane with half of the width of the other two models, where the top edge is located at almost 500 m depth. The dip is significantly smaller for Model 1 and Model 3, with ~53° and ~59°, respectively. Due to the smaller area of the fault plane in Model 2, the slip in dip direction is two and three times larger with respect to Model 1 and Model 3.

The models calibrated with a single dataset show very good fit with the ascending (Figure 5a) and descending (Figure 5f) interferograms separately. In case of the two datasets inverted simultaneously (Figure 5d,i), misfits increase (Figure 5e,j), especially with the descending data.

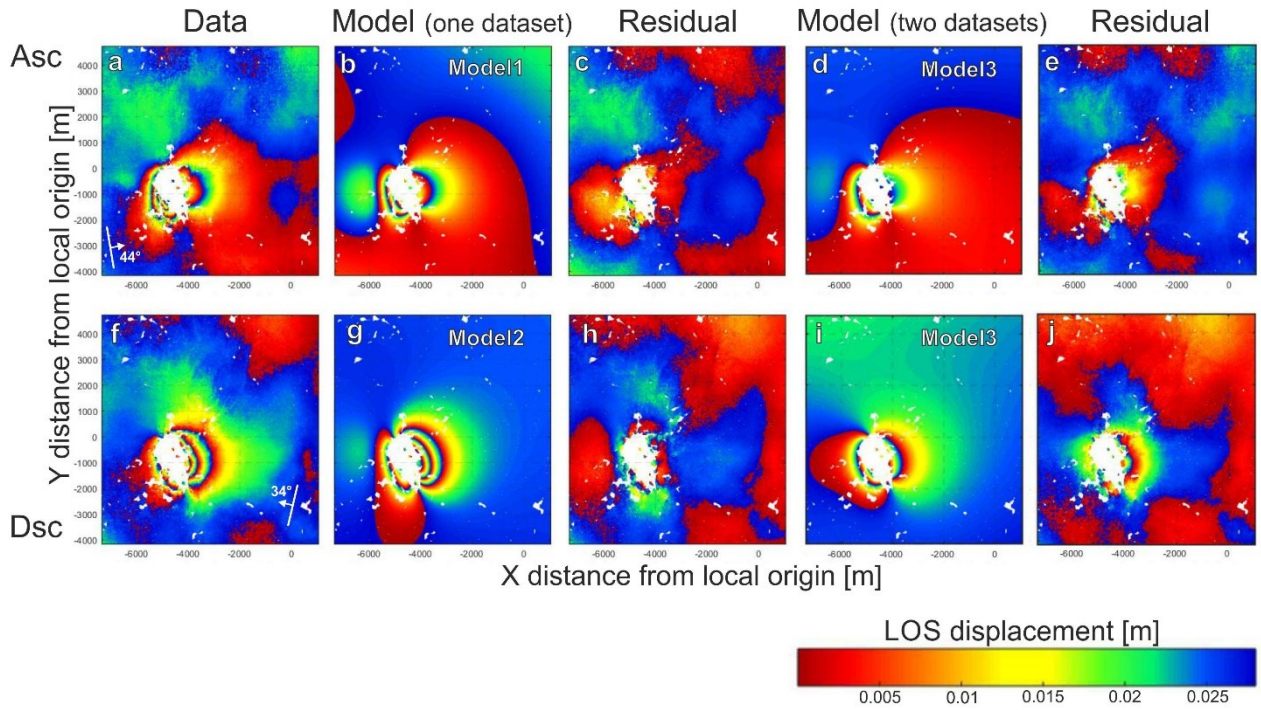

Figure 5: Observed (a, f), modeled (b, d, g, i), and residual (c, e, h, j) displacements in the LOS direction for ascending (top) and descending (bottom) satellite passes, mapping the coseismic deformation of the 8 February 2016 earthquake. Arrows in a and f indicate the flight direction of the satellite and the look direction with the corresponding incidence angles. Model 1 and Model 2 are obtained by the inversion of the ascending and descending interferograms separately. For Model 3 the two interferograms were used simultaneously.

Table 2: Prior values and inversion results of the source parameters of the 8 February 2016 earthquake at Los Humeros. 2.5 and 97.5 percentiles of posterior probability density functions of the fault parameters are reported. For Model 1 and Model 2 we employed the ascending and descending datasets respectively. Model 3 was constructed based on the joint inversion of the two interferograms. Note that the strike and dip ranges are selected in order to fix the position of the midpoint of the top edge of the fault plane (see Bagnardi and Hooper 2018).

	Total Model Range		Model 1	Model 2	Model 3
	Lower	Upper	Optimal (2.5% – 97.5%)	Optimal (2.5% – 97.5%)	Optimal (2.5% – 97.5%)
Top Depth [m]	0	2000	2.08 (0.034 – 3.82)	485.03 (485.03 – 485.03)	0.89 (0.26 – 3.86)
Dip [°]	-90	-45	-52.57 (-54.09 – -51.40)	-90.00 (-90.00 – -90.00)	-58.92 (-60.67 – -58.08)
Strike [°]	270	360	341.74 (341.14 – 341.89)	334.72 (334.72 – 334.72)	339.74 (339.66 – 340.48)
Length [m]	1000	2500	1489.13 (1455.18 – 1512.77)	1814.51 (1814.51 – 1814.51)	1655.46 (1632.21 – 1678.68)
Width [m]	500	2000	1141.72 (1108.34 – 1185.52)	517.35 (517.35 – 517.35)	1301.08 (1249.40 – 1372.38)
X center [m]	-4650	-4450	-4534.55 (-4538.58 – -4533.69)	-4631.75 (-4631.75 – -4631.75)	-4529.56 (-4535.18 – -4529.14)
Y center [m]	-1000	-800	-865.54 (-867.06 – -853.84)	-992.72 (-992.72 – -992.71)	-844.09 (-844.73 – -839.78)
Strike slip [m]	-0.5	0.5	-0.055 (-0.072 – -0.052)	0.0720 (0.035 – 0.128)	-0.052 (-0.062 – -0.045)
Dip slip [m]	-2.0	2.0	-0.284 (-0.296 – -0.271)	-0.638 (-0.652 – -0.614)	-0.180 (-0.184 – -0.173)

4. DISCUSSION AND CONCLUSIONS

The PS-InSAR analysis shows that the LHGF is characterized by up to 8 mm/year of subsidence during the period of the InSAR monitoring (Fig. 5). We attribute this deformation to field operations given that the estimated maximum subsidence is located around the production wells. Given the concentration of deformation around the wells, the estimated source depth and the short wavelength deformation pattern, we think that the estimated deformation is primarily due to geothermal production and not volcano-tectonic related. The area of maximum subsidence is relatively small, located at the northern part of the geothermal field. This area appears to be isolated from the injection wells that were operational during the period of the InSAR analysis. This isolation is supported by the epicenters of the induced earthquakes [Urban and Lerno, 2013], most of which are located west from the injectors, suggesting that the majority of the injected fluids are directed westwards (Fig. 5b). No clear subsidence signal is observed in the southern and western part of the field, although large numbers of production wells have been drilled in these areas. This indicates a significant pressure support that might originate from deep recharge and partly from the injected volumes. Pressures cannot be supported only by the injectors, since the injected volumes are about ten times smaller than the produced volumes. The pressure support by underlying aquifers is corroborated by the large difference in modeled rock compaction volume from the inversion exercise and the volume of net produced fluids. Regional recharge outside the study area through deep structures may contribute to the recovery of the extracted fluid volume.

The InSAR data together with the modeling results also suggest that the Los Humeros geothermal field is controlled by sealing faults that separate the reservoir into several blocks. However, additional subsurface data, for instance regular pressure measurements from the wells, are needed to improve our modelling results. This would also allow us to study fault sealing behavior that controls reservoir compartmentalization. Still, our results make clear that based on the subsidence pattern, we have obtained a

better understanding of the pressure conditions within the reservoir and potential local recharge zones. This will facilitate better quality decisions on well planning and operations. Additionally, the surface deformation pattern can contribute to our understanding on superhot geothermal systems, which are of high potential for geothermal energy development.

The occurrence of induced seismicity is independent evidence for the development of effective stresses. The inversion of the coseismic deformation due to the 8 February 2016 earthquake showed activation of a shallow normal fault in a reverse manner. This was in line with the coseismic deformation mapped by Santos-Basurto et al [2018]. Even with the limited compaction observed from the subsidence, the stress development was enough to induce seismicity. Pore pressure contrasts over a fault will increase the stress development (Van Wees et al, 2017). However, fault structures will be more complex than assumed in the present study, because an acceptable joint match of ascending and descending surface movement data was not possible. An integrated study into the complex reservoir behaviour and the associated stress development over complex faults is therefore warranted. That would allow us to study the connection between volcanotectonic activity and geothermal energy production targeting superhot geothermal systems.

ACKNOWLEDGEMENTS

The project leading to the results in this article received funding from the European Union's Horizon 2020 research and innovation programme under grant agreement No. 727550 (GEMex).

REFERENCES

Atzori, S., Hunstad, I., Chini, M., Salvi, S., Tolomei, C., Bignami, C., ... & Boschi, E. (2009). Finite fault inversion of DInSAR coseismic displacement of the 2009 L'Aquila earthquake (central Italy). Geophysical Research Letters, 36(15).

Bagnardi, M., Hooper, A. (2018). Inversion of surface deformation data for rapid estimates of source parameters and uncertainties: A Bayesian approach. Geochemistry, Geophysics, Geosystems,, 19(7), 2194-2211

Békési, E., Fokker, P. A., Martins, J. E., Limberger, J., Bonté, D., & van Wees, J. D. (2019a). Production-Induced Subsidence at the Los Humeros Geothermal Field Inferred from PS-InSAR. Geofluids.

Békési, E., Fokker, P.A. Esteves Martins, J, van Wees, J.D. (2019b) Inversion of coseismic deformation due to the 8th February 2016, Mw 4.2 earthquake at Los Humeros (Mexico) inferred from DInSAR. Presented at the European Geothermal Congress, The Hague, June.

Carrasco-Núñez, G., López-Martínez, M., Hernández, J., & Vargas, V. (2017) Subsurface stratigraphy and its correlation with the surficial geology at Los Humeros geothermal field, eastern Trans-Mexican Volcanic Belt. *Geothermics* 67, 1-17.

Ferretti, A. (2014). Satellite InSAR data: reservoir monitoring from space. EAGE publications.

Ferriz, H., Mahood, G.: Eruption rates and compositional trends at LosHumeros volcanic center, puebla, Mexico, (1984) J. Geophys. Res., 89 (B10),8511–8524.

Hanssen, R. F. (2001). Radar interferometry: data interpretation and error analysis (Vol. 2). Springer Science & Business Media.

Lermo Samaniego, J. F., Lorenzo, C., Antayhua, Y., Ramos, E., & Jiménez, N. (2016). Sísmica pasiva en el campo geotérmico de los Humeros, Puebla-México y su relación con los pozos inyectores. *XVIII Congreso Peruano de Geología 2016*, Sociedad Geológica del Perú, Lima, Perú, p. 5.

Mindlin, R.D. (1936), Force at a point in the interior of a semi-infinite solid, Physics, Vol. 7, No. 5, pp. 195-202

Okada, Y. (1985). Surface deformation due to shear and tensile faults in a half-space. Bulletin of the Seismological Society of America, Vol. 75, No. 4, pp. 1135-1154

Norini, G., Groppelli, G., Sulpizio, R., Carrasco- Núñez, G., Davila-Harris, P., Pellicioli, C., Zucca, F., De Franco, R. (2015) Structural analysis and thermal remote sensing of the Los Humeros Volcanic Complex: implications for volcano structure andgeothermal exploration. J. Volcanol. Geotherm. Res., 301, 221–237.

Santos-Basurto, R., Sarychikhina, O., López-Quiroz, P., Norini, G., Carrasco-Núñez, G. (2018) The Mw 4.2 (February 8th, 2016) earthquake detected inside of Los Humeros caldera, Puebla-Mexico, by means of DInSAR. European Geosciences Union 2018, Vienna, Austria, poster 18431.

Segall, P. (2010) Earthquake and volcano deformation, p. 430.

Urban, E. and Lermo, J. F. (2013) Local seismicity in the exploitation of Los Humeros geothermal Field, Mexico," Proceedings of thirty-eighth workshop on geothermal reservoir engineering.

van Wees, J. D., Osinga, S., Van Thienen-Visser, K., & Fokker, P. A. (2017). Reservoir creep and induced seismicity: inferences from geomechanical modeling of gas depletion in the Groningen field. *Geophysical Journal International*, *212*(3), 1487-1497.

Wegmüller, U., Werner, C. (1997). Gamma SAR processor and interferometry software. Proceedings of the 3rd ERS Symposium 1997, Florence, Italy, 14–21.